

This is the accepted manuscript made available via CHORUS. The article has been published as:

## Temperature dependence of phonons in Pd<sub>3</sub>Fe through the Curie temperature

F. C. Yang, O. Hellman, M. S. Lucas, H. L. Smith, C. N. Saunders, Yuming Xiao, Paul Chow, and B. Fultz

Phys. Rev. B **98**, 024301 — Published 3 July 2018

DOI: [10.1103/PhysRevB.98.024301](https://doi.org/10.1103/PhysRevB.98.024301)

# The temperature dependence of phonons in $\text{Pd}_3\text{Fe}$ through the Curie temperature

F. C. Yang,<sup>1</sup> O. Hellman,<sup>1</sup> M. S. Lucas,<sup>1</sup> H. L. Smith,<sup>1</sup> C. N. Saunders,<sup>1</sup> Yuming Xiao,<sup>2</sup> Paul Chow,<sup>2</sup> and B. Fultz<sup>1</sup>

<sup>1</sup>*Applied Physics and Materials Science, California Institute of Technology, Pasadena, CA 91125*

<sup>2</sup>*HPCAT, Geophysical Laboratory, Carnegie Institution of Washington, Argonne, Illinois, 60439, USA*

Iron phonon partial densities of states (pDOS) of  $\text{Pd}_3^{57}\text{Fe}$  were measured from room temperature through the Curie transition at 500 K using nuclear resonant inelastic x-ray scattering. The experimental results were compared to *ab initio* spin-polarized calculations that model the finite temperature thermodynamic properties of  $L1_2$ -ordered  $\text{Pd}_3\text{Fe}$  with stochastically-generated atomic displacements, coupled with magnetic special quasirandom structures (SQSs) of noncollinear magnetic moments. The scattering measurements and first-principles calculations show that the Fe partial vibrational entropy is close to what is predicted by the quasiharmonic approximation owing to a cancellation of effects. Anharmonicity and a magnon-phonon interaction approximately cancel a ferromagnetic optical phonon stiffening.

## I. INTRODUCTION

Advances in the design of magnetic materials are enabled by understanding how their properties depend on the external conditions of temperature, pressure, and magnetic field. In particular, it is important to understand their thermodynamic properties over a range of temperatures. This requires modeling a magnetic material not only in its ground state at 0 K, but also in its magnetically disordered states at finite temperatures.

Progress has been made in first-principles simulations of magnetic disorder in materials [1]. Recent approaches to modeling the paramagnetic state of magnetic materials include disordered local moment molecular dynamics (DLM-MD) [2, 3], spin-space averaging [4–7], and spin dynamics [8–10]. With such advances, a computational study accounting for the interaction of the magnetic and atomic degrees of freedom, which has been demonstrated to provide a more complete calculation of the Gibbs free energy of magnetic materials [11], is now within reach. In the present study of the thermal excitations in  $\text{Pd}_3\text{Fe}$ , magnetic disorder is included in the finite temperature calculations of vibrational thermodynamic properties.

Fe–Pd alloys have been a subject of numerous studies owing to their magnetic and mechanical behavior. Properties of interest include a martensitic transformation in Fe-rich alloys [7, 12, 13], noncollinear magnetic structures [14–17], and Invar behavior [18].  $\text{Pd}_3\text{Fe}$ , a ferromagnetic metallic compound with an fcc-based  $L1_2$  structure and a Curie temperature of approximately 500 K [19], exhibits Invar behavior under an applied pressure [20]. This compound also exhibits an anomalous dependence of phonon frequencies and volume with pressure as a consequence of a magnetic transition [16, 21]. In this present work, we investigate this interaction between lattice dynamics and magnetic excitations at temperatures through the Curie temperature, using nuclear resonant inelastic x-ray scattering and first-principles calculations.

## II. METHODS

### A. Experiment

Measurements were performed on the  $L1_2$ -ordered  $\text{Pd}_3^{57}\text{Fe}$  sample used in a pressure-induced Invar experiment [20], which was prepared by arc-melting Pd of 99.95% purity and  $^{57}\text{Fe}$  of 95.38% isotopic enrichment before being cold rolled to a thickness of 25  $\mu\text{m}$ . This ordered sample was further annealed with a heat treatment at 873 K for 18 hours under vacuum, 773 K for 54 hours, and subsequent cooling to 293 K over 2 hours. X-ray diffraction confirmed the  $L1_2$  structure and long-range order, and Mössbauer spectroscopy confirmed the short-range order (shown in the Supplemental Material [22]).

Nuclear resonant inelastic x-ray scattering (NRIXS) measurements were performed on  $\text{Pd}_3^{57}\text{Fe}$  at seven temperatures from 298 to 786 K. NRIXS is a low background technique that provides direct access to the phonon partial density of states (pDOS) of  $^{57}\text{Fe}$  [24, 25]. Measurements were performed at beamline 16ID-D of the Advanced Photon Source at Argonne National Laboratory. The synchrotron flashes had durations of 70 ps and were separated by 153 ns. Electronic scattering occurs within femtoseconds of the pulse arrival at the sample. The relatively long lifetime of the nuclear resonant state ( $\tau = 141$  ns) allowed for a clear separation of the prompt electronic scattering from the delayed resonant scattering.

The  $\text{Pd}_3^{57}\text{Fe}$  foil sample was held in vacuum under active evacuation in a resistive heating furnace with a kapton window for x-ray transmission. Errors in the values of the temperature ranged from  $\pm 10$  to  $\pm 27$  K. The ambiguity comes from comparing the furnace thermocouple measurements to NRIXS-derived detailed balance temperature calculations following procedure described in the literature [26, 27].

An avalanche photodiode was positioned at approximately  $90^\circ$  from the incident beam to collect incoherently reradiated photons. The energy was scanned from  $-80$  to  $+80$  meV around 14.413 keV, the resonant energy of  $^{57}\text{Fe}$ , in several scans that were combined for final analysis. The energy resolution of all NRIXS measurements

was measured to be 2.2 meV (FWHM) at the elastic line. The PHOENIX software package was used to extract the  $^{57}\text{Fe}$  pDOS from the measured NRIXS spectra [26].

Nuclear forward scattering (NFS) measurements were collected immediately prior to NRIXS scans. The NFS spectra provide a measure of the magnetic state of  $\text{Pd}_3^{57}\text{Fe}$ , using an avalanche photodiode in the path of the forward-scattered x-ray beam to measure the transmitted intensity as a function of time.

In situ synchrotron x-ray diffraction (XRD) measurements were performed concurrently with the NRIXS and NFS measurements with the same monochromatic beam of 14.413 keV x-rays and a Mar CCD detector plate. Results from synchrotron XRD were used to obtain lattice parameters for the quasiharmonic (QH) approximation of the Fe pDOS.

## B. Computational: Phonon Calculation

Phonon frequencies at elevated temperatures were calculated with a variation of the temperature dependent effective potential (TDEP) method [29–31]. In the TDEP procedure, the Born-Oppenheimer surface of a material at a given temperature is sampled with *ab initio* molecular dynamics (AIMD). The energies, displacements, and forces on thermally-displaced atoms are recorded over time. With these energy-force-displacement datasets, force constants are obtained with a least-squares fit of the following model Hamiltonian to the potential energy surface at a given temperature

$$\mathcal{H} = U_0 + \frac{1}{2!} \sum_{ij\alpha\beta} \Phi_{ij}^{\alpha\beta} u_i^\alpha u_j^\beta + \frac{1}{3!} \sum_{ijk\alpha\beta\gamma} \Phi_{ijk}^{\alpha\beta\gamma} u_i^\alpha u_j^\beta u_k^\gamma, \quad (1)$$

where  $u_i$  is the displacement of atom  $i$  and  $\alpha\beta\gamma$  are Cartesian components. The temperature-dependent  $U_0$  is a fit parameter for the baseline of the potential energy surface [30]. The quadratic force constants  $\Phi_{ij}$  from the thermally-displaced atoms capture nonharmonic effects such as magnon-phonon interactions at a given temperature, and are used to calculate phonon frequencies  $\omega_s$  shifted by these effects [30], where  $s$  is an index for phonon modes. The cubic force constants  $\Phi_{ijk}$  capture phonon-phonon interactions (PPI) that contribute to the broadening and additional shifts of phonon modes [31].

The same procedure was applied in this work, except the Born-Oppenheimer surface was sampled through multiple DFT calculations on supercells of thermally-displaced atoms generated by stochastic sampling of a canonical ensemble. For a cell of  $N_a$  atoms with mass  $m_i$ , a harmonic normal mode transformation was used to generate positions  $\{u_i\}$  consistent with a canonical ensemble:

$$u_i = \sum_{s=1}^{3N_a} \epsilon_{is} \langle A_{is} \rangle \sqrt{-2 \ln \xi_1} \sin(2\pi \xi_2), \quad (2)$$

where  $\omega_s$  and  $\epsilon_{is}$  are the eigenvalues and eigenvectors of phonon modes  $s$  obtained from trial force constants calculated from short AIMD simulations. Other quantities include  $\xi_n$ , uniformly distributed random numbers between 0 and 1 producing the Box-Muller transform, and  $\langle A_{is} \rangle$ , the thermal average of the normal mode amplitudes [33, 34]:

$$\langle A_{is} \rangle = \underbrace{\sqrt{\frac{\hbar(2n_s + 1)}{2m_i\omega_s}}}_{\text{quantum}} \approx \underbrace{\frac{1}{\omega_s} \sqrt{\frac{k_B T}{m_i}}}_{\text{classical}}, \quad (3)$$

where  $n_s = (e^{\hbar\omega_s/k_B T} - 1)^{-1}$  is the thermal occupation of mode  $s$ , and  $\hbar\omega \ll k_B T$  denotes the classical limit at high temperatures. These stochastically generated thermal displacements from Eqs. 2 and 3 sample the Born-Oppenheimer surface in the stochastically-initialized temperature dependent effective potential (s-TDEP) method [29–32].

This method approximates the inclusion of zero-point motion not included in AIMD simulations, and connects seamlessly to the classical limit at high temperature. The s-TDEP procedure can be used to calculate force constants capturing anomalous high temperature effects [32] to low temperature quantum effects [35, 36] at a much lower computational cost than what is required of AIMD. The force constants calculated with this method are numerically converged with respect to the number of configurations and supercell size. Fewer configurations would be required if the size of the supercell were larger. The convergence of the force constants and the baseline  $U_0$  was further ensured by repeating DFT calculations on new snapshots generated by Eq. 2, where the frequencies  $\omega_s$  were calculated from the force constants from the previous iteration of s-TDEP. The weakness of the s-TDEP method is that it relies on Gaussian distributions of coordinates generated by Eq. 2.

The *ab initio* spin-polarized density functional theory (DFT) calculations with spin-orbit coupling were performed with the projector augmented wave [37] formalism as implemented in VASP [38, 39]. All calculations used a  $3 \times 3 \times 3$  supercell with 108 atoms, a  $2 \times 2 \times 2$  Monkhorst-Pack [40]  $k$ -point grid, and a plane wave energy cutoff of 520 eV. The exchange-correlation energy was calculated with the Perdew-Burke-Ernzerhof (PBE) functional [41]. It was observed from calculations and from past experiments [42–44] that the magnetic moment of Pd atoms in  $\text{Pd}_3\text{Fe}$  is small compared to that of Fe atoms. The Pd moments were approximated as zero.

At a given temperature, the forces and energies of 25 stochastically-generated supercells were calculated at five volumes within  $-2.5$  to  $+5\%$  around the 0 K equilibrium volume through three iterations of the s-TDEP procedure. For each volume, the Helmholtz free energy  $F(V, T)$  was calculated:

$$F(V, T) = U_0(V, T) + F_{\text{vib}}(V, T). \quad (4)$$

$U_0(V, T)$  is the baseline from Eq. 1.  $F_{\text{vib}}(V, T)$  is from

lattice vibrations:

$$F_{\text{vib}} = \int_0^\infty g(\omega) \left\{ k_B T \ln \left[ 1 - \exp \left( -\frac{\hbar\omega}{k_B T} \right) \right] + \frac{\hbar\omega}{2} \right\} d\omega, \quad (5)$$

where  $g(\omega)$  is the phonon density of states calculated from the phonons in the first Brillouin zone:

$$g(\omega) = \sum_s \delta(\omega - \omega_s). \quad (6)$$

At a given temperature, the equilibrium volume  $V_T$  was obtained through the minimization of the Helmholtz free energy  $F(T, V)$ . The force constants were then interpolated to this volume, giving us phonon frequencies that capture volume expansion and temperature-dependent nonharmonic effects.

We then corrected our phonon frequencies  $\omega_s(T, V_T)$  by calculating the linewidths  $\Gamma_s$  and shifts  $\Delta_s$  arising from anharmonicity, or phonon-phonon interactions. This required the many-body perturbation calculation of the real and imaginary parts of the phonon self-energy [45, 46]  $\Sigma(\Omega) = \Delta(\Omega) + i\Gamma(\Omega)$ , where  $E = \hbar\Omega$  is a probing energy. The imaginary component  $\Gamma(\Omega)$  is

$$\begin{aligned} \Gamma_s(\Omega) = & \frac{\hbar\pi}{16} \sum_{s's''} |\Phi_{ss's''}|^2 \{ (n_{s'} + n_{s''} + 1) \\ & \times \delta(\Omega - \omega_{s'} - \omega_{s''}) + (n_{s'} - n_{s''}) \\ & \times [\delta(\Omega - \omega_{s'} + \omega_{s''}) - \delta(\Omega + \omega_{s'} - \omega_{s''})] \}, \quad (7) \end{aligned}$$

and the real component is obtained by a Kramers-Kronig transformation

$$\Delta(\Omega) = \frac{1}{\pi} \int \frac{\Gamma(\omega)}{\omega - \Omega} d\omega. \quad (8)$$

The imaginary component of the self-energy is a sum over all possible three-phonon interactions, where  $\Phi_{ss's''}$  is the three-phonon matrix element determined from the cubic force constants  $\Phi_{ijk}$ .  $\Gamma(\Omega)$  and  $\Delta(\Omega)$  were calculated with a  $36 \times 36 \times 36$   $q$ -grid.

Anharmonic phonon DOS curves were calculated with the real and imaginary parts of the phonon self-energy:

$$g_{\text{anh}}(\omega) = \sum_s \frac{2\omega_s \Gamma_s(\omega)}{[\omega^2 - \omega_s^2 - 2\omega_s \Delta_s(\omega)]^2 + 4\omega_s^2 \Gamma_s^2(\omega)}. \quad (9)$$

It is noted that if both  $\Delta$  and  $\Gamma$  go to zero, Eq. 9 reduces to Eq. 6.

This procedure was implemented to calculate two sets of phonon dispersions and DOS: for  $\text{Pd}_3\text{Fe}$  maintaining complete ferromagnetic order at 0, 300, 480, 600, and 800 K (illustrated with Fig. 1(a)), and for  $\text{Pd}_3\text{Fe}$  with increasing magnetic disorder at 300, 480, and 800 K (illustrated with Fig. 1(b)).  $\text{Pd}_3\text{Fe}$  is expected to be completely ferromagnetic only at 0 K. The calculations of the completely ferromagnetic  $\text{Pd}_3\text{Fe}$  at nonzero temperatures were performed for comparison with computations with magnetic disorder.

For comparison with the s-TDEP phonon spectra, the phonon energies predicted by the quasiharmonic (QH) approximation were calculated by interpolation of the 0 K quadratic force constants to volumes obtained from the minimization of the free energy. This “QH DFT model” assumes that the only temperature dependence in Eq. 4 and 5 is from volume expansion and the Planck distribution. The “QH DFT model” excludes the anharmonic corrections provided by Eqs. 7 and 8.

### C. Computational: Magnetic Disorder

The magnetic disorder from thermal fluctuations was modeled with special quasirandom structures (SQSs) [47] of noncollinear Fe magnetic moments. The magnetic SQSs mimic the most relevant local correlation functions of random magnetic structures [48], where the correlation function of the coordination shell  $\alpha$  is

$$\Pi_\alpha = \frac{1}{N_\alpha} \sum_{i,j \in \alpha} \mathbf{e}_i \cdot \mathbf{e}_j, \quad (10)$$

where  $\mathbf{e}_i = \mathbf{m}_i / \|\mathbf{m}_i\|$  is a unit vector in the direction of the magnetic moment  $\mathbf{m}_i$  on site  $i$ , and  $N_\alpha$  is the number of magnetic moment pairs in the coordination shell  $\alpha$ . This use of SQSs with noncollinear Fe magnetic moments is related to the disordered local moment (DLM) model, where magnetic disorder is modeled with randomly oriented local magnetic moments [49–54].

A histogram of magnetic SQSs was generated by simulated annealing, where Fe magnetic moments were flipped into random orientations until the local correlation functions matched target correlation functions. These bins were of increasing levels of magnetic disorder, from completely ordered to completely disordered. In the same bin of the histogram, the set of magnetic SQSs  $\{\lambda\}$  were equivalent in their correlation functions.

All correlation functions of magnetic SQSs modeling complete ferromagnetic order equaled 1 ( $\Pi_\alpha = 1, \forall \alpha$ ), and the resulting Fe magnetic moments were aligned in the same direction. All correlation functions of magnetic SQSs modeling complete magnetic disorder equaled 0 ( $\Pi_\alpha = 0, \forall \alpha$ ), and the resulting Fe magnetic moments were randomly oriented. The correlation functions for magnetic SQSs from a bin that was between complete order and complete disorder had values between 0 and 1. For a given bin, the generated magnetic SQSs had an averaged normalized magnetization

$$\langle M/M_0 \rangle_{\text{SQS}} = \frac{1}{N_m} \left\| \sum_\lambda \left( \sum_i \mathbf{m}_i \right) \right\|, \quad (11)$$

where  $N_m$  is a normalization constant.

For the phonon calculations of  $\text{Pd}_3\text{Fe}$  with increasing magnetic disorder, we coupled the s-TDEP procedure with these magnetic SQSs. For a given temperature  $T$ , 25 stochastically sampled supercells  $\{\kappa\}$  with thermal

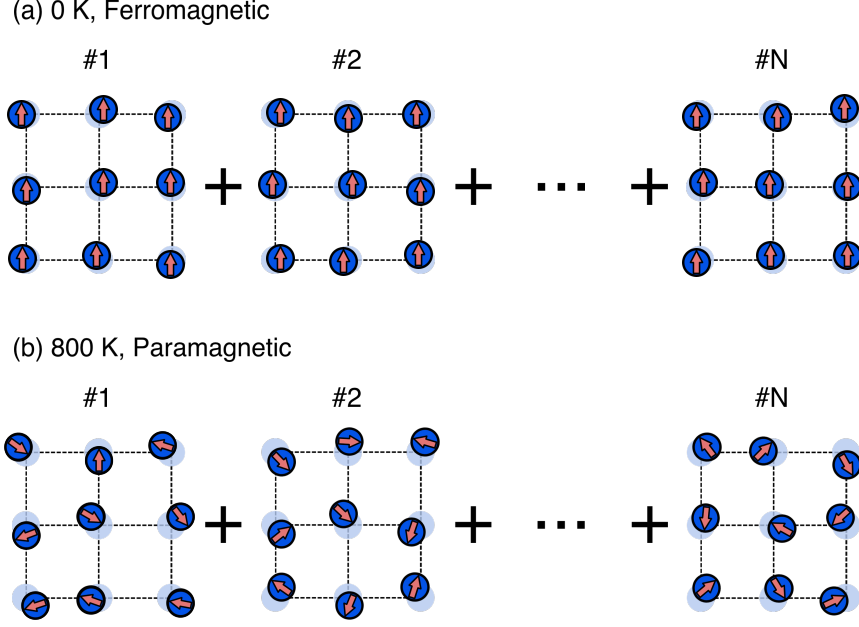


FIG. 1. (a) Schematic of supercells with Fe atoms (dark blue) stochastically displaced from their ideal positions (light blue) in the 0 K ferromagnetic calculations, where the magnetic moments (red arrows) are aligned in the same direction. (b) Supercells with randomly oriented magnetic moments and stochastically displaced Fe atoms in the 800 K paramagnetic calculations. Each set of randomly oriented magnetic moments is a magnetic special quasirandom structure (SQS). Pd atoms are not shown for this illustration.

atomic displacements characteristic of  $T$  were generated. Separately, 25 magnetic SQSs  $\{\lambda\}$  were selected from a bin where the SQSs have an averaged normalized magnetization  $\langle M/M_0 \rangle_{\text{SQS}}$  approximately equal to the normalized magnetization  $M(T)/M_0$  expected at temperature  $T$ . A spin-polarized DFT calculation was performed on a supercell  $\kappa$  paired with a magnetic SQS  $\lambda$ . The forces from these spin-polarized DFT calculations on the ensemble of SQS-supercell  $(\kappa, \lambda)$  pairs, illustrated in Fig. 1b, are used to obtain force constants used in the calculation of phonon dispersions and DOS, as described previously. This computational method can be considered to be a stochastic ensemble-averaged variant of disordered local moments molecular dynamics (DLM-MD) [2, 3] with local spin correlations.

For the calculations at 800 K, the magnetic structure was treated as a random distribution of magnetic moments characterized by the vanishing of the spin correlation functions ( $\Pi_\alpha = 0, \forall \alpha$ ) so that the average magnetization  $\langle M \rangle_{\text{SQS}}$  is zero, in accordance with the DLM model. The force constants calculated at 800 K were interpolated to a volume that minimized a modified Helmholtz free energy  $F(T, V)$

$$F(T, V) = U_0(T, V) + F_{\text{vib}}(T, V) + F_{\text{mag}}(T, V), \quad (12)$$

where  $F_{\text{mag}}(T, V)$  is the magnetic free energy. Because there is no exact formulation for the magnetic free energy, this free energy was approximated with a mean-field term

$$F_{\text{mag}}(T, V) = -TS_{\text{mag}} = -k_B T \ln(\langle m(V) \rangle + 1), \quad (13)$$

where  $\langle m(V) \rangle$  is the average magnitude of the magnetic moments in units of  $\mu_B$ . The magnetic entropy  $S_{\text{mag}}$  is the maximum orientational disorder of magnetic moments in the paramagnetic state for systems with local magnetic moments. This approach is widely used to describe the magnetic entropy of paramagnetic systems [6, 55].

For calculations at 300 and 480 K, the magnetic structures were sampled so the averaged normalized magnetizations  $\langle M/M_0 \rangle_{\text{SQS}}$  were approximately equal to normalized hyperfine fields  $H(T)/H_0$  obtained from Mössbauer spectroscopy measurements performed in this study and by Longworth [19], as seen in Fig. 3. Because there is no reliable method for calculating the magnetic free energy of  $\text{Pd}_3\text{Fe}$  at intermediate temperatures, force constants were calculated at volumes obtained by scaling the volume calculated at 800 K by volumes obtained from synchrotron x-ray diffraction measurements.

### III. RESULTS

#### A. Nuclear Forward Scattering

The NFS spectra measured from the  $\text{Pd}_3^{57}\text{Fe}$  sample are shown in Fig. 2. The NFS spectrum at 298 K exhibits a clear magnetic beat pattern expected from a magnetically-ordered material, similar to a previous NFS measurement of  $\text{Pd}_3^{57}\text{Fe}$  at ambient conditions [20]. The

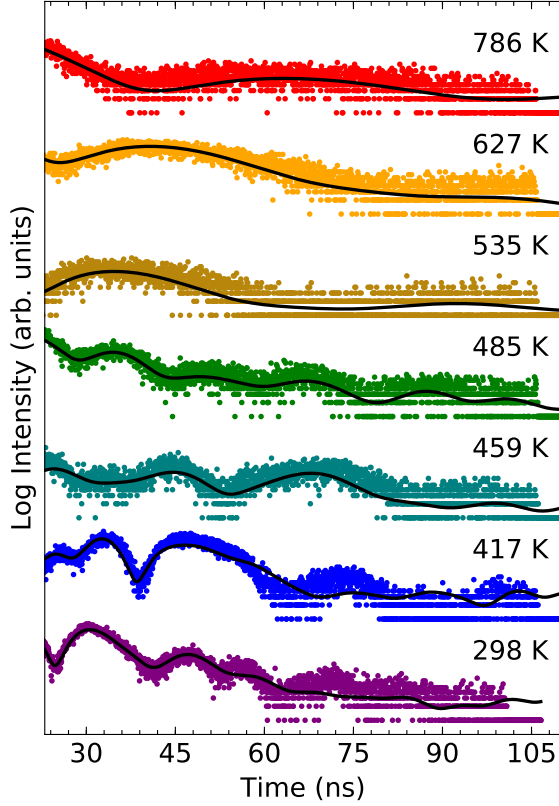


FIG. 2. The  $^{57}\text{Fe}$  nuclear forward scattering spectra from  $L_{12}$ -ordered  $\text{Pd}_3\text{Fe}$  at several temperatures. The fits (black curves) overlay experimental data (points). The spectra are displayed using a log scale, and offset for clarity.

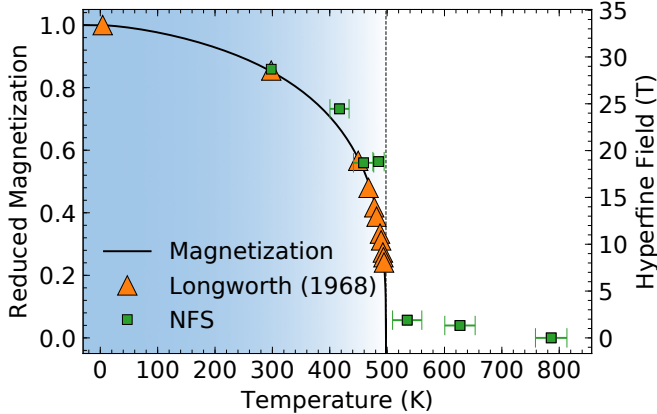


FIG. 3. The magnetization curve of  $\text{Pd}_3\text{Fe}$  obtained from an empirical fit of a magnetic shape function [56] to hyperfine magnetic fields obtained from the NFS spectra in this study (green) and Mössbauer data from a study by Longworth [19] (orange). The shaded region indicates the temperature range where  $\text{Pd}_3\text{Fe}$  exhibits ferromagnetic order.

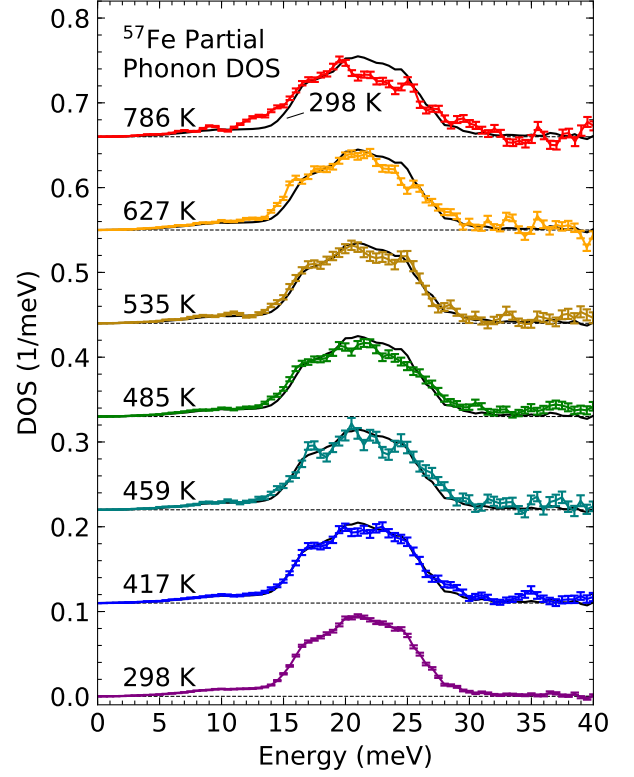


FIG. 4. The normalized  $^{57}\text{Fe}$  pDOS extracted from NRIXS measurements at various temperatures. The spectra from measurements above 298 K are offset and compared with the 298 K pDOS (black curve). Error bars are from counting statistics.

amplitudes and periods of the magnetic beats diminish with temperature, and the magnetic beats disappear above 485 K, consistent with a second-order phase transition in which the magnetic order continuously decreases through the Curie temperature. The remaining beats above 485 K are from the thickness of the sample.

A quantitative analysis of the NFS spectra was performed with the software package CONUSS [26, 57]. The refined fits overlay the experimental spectra in Fig. 2. Parameters extracted from these fits include the hyperfine field  $H$ , shown together with the magnetization of  $\text{Pd}_3\text{Fe}$  in Fig. 3, and the Lamb-Mössbauer factor, shown in the Supplemental material [22]. The decrease in the hyperfine field of  $\text{Pd}_3^{57}\text{Fe}$  with temperature is in agreement with the hyperfine fields measured by Longworth [19], and the decrease in this quantity with temperature tracks the decrease in magnetization through the Curie temperature.

## B. Phonons

The  $^{57}\text{Fe}$  pDOS curves measured from the  $\text{Pd}_3^{57}\text{Fe}$  sample are shown in Fig. 4. The pDOS do not show significant energy shifts below the Curie temperature. The

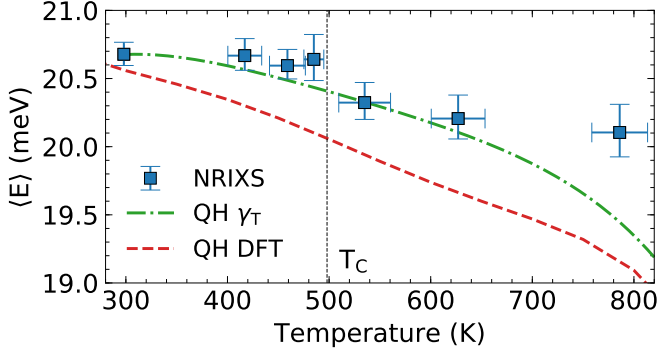


FIG. 5. Average energies of the Fe pDOS from NRIXS measurements (blue points) plotted with the average Fe phonon energies from the Grüneisen parameter model (green line) and the QH DFT model (red line).

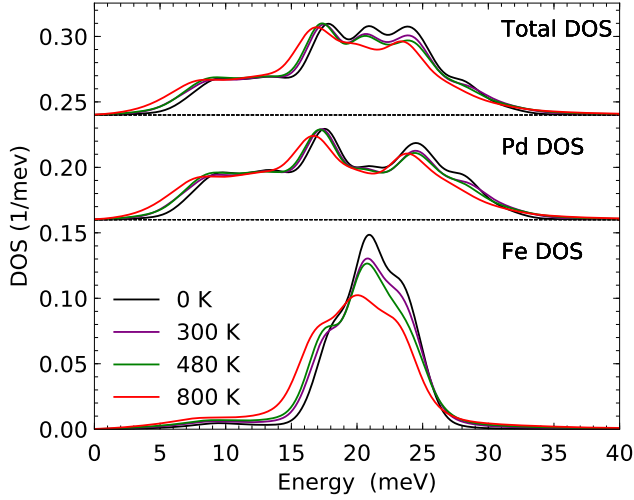


FIG. 6. Total, Pd partial, and Fe partial phonon DOS curves of  $\text{Pd}_3\text{Fe}$  calculated with the s-TDEP method from 0 to 800 K.

phonons begin to show a small but significant thermal softening beyond the Curie temperature, made apparent when the 627 and 786 K pDOS are compared with the 298 K curve in Fig. 4. This trend is seen more clearly with the average Fe phonon energies calculated from the  $^{57}\text{Fe}$  pDOS, shown in Fig. 5. These phonon shifts are similar to the experimental trends observed in the ferromagnetic cementite through the Curie temperature [58]. It is noted that the quality of the high temperature  $^{57}\text{Fe}$  pDOS at 786 K was impacted by reduced counting statistics.

The phonon DOS curves calculated at 0, 300, 480, and 800 K with s-TDEP are shown in Fig. 6. The phonon DOS curves soften with temperature, although features like the peak at 21 meV in the Fe pDOS or at 25 meV in the Pd pDOS do not soften until the Curie temperature. The s-TDEP phonon DOS curves also exhibit a thermal broadening that is most prominent at 800 K, indicative of phonon-phonon interactions (PPI) [45, 46, 59, 60].

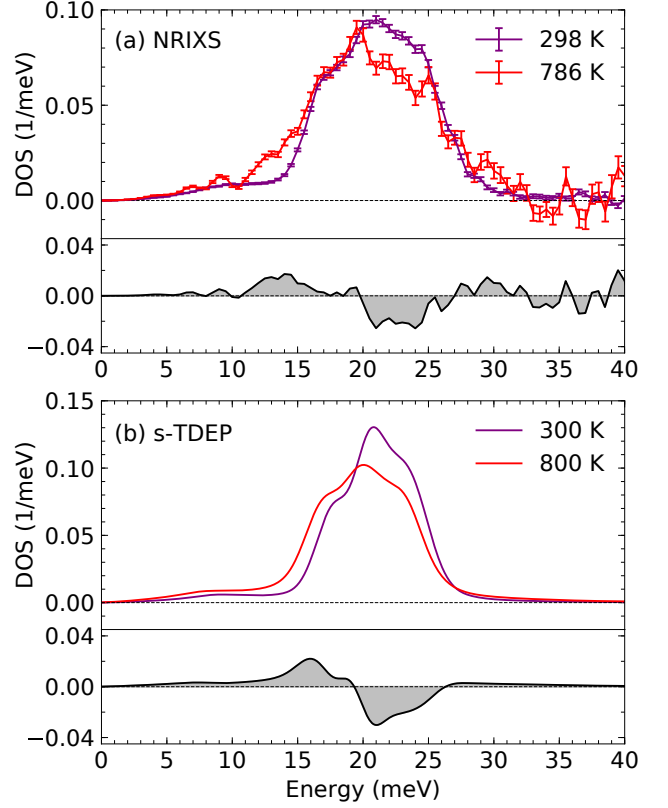


FIG. 7. (a) NRIXS  $^{57}\text{Fe}$  pDOS curves compared at 298 and 786 K. (b) s-TDEP Fe pDOS curves compared at 300 and 800 K. Phonon difference spectra are shown for both NRIXS and s-TDEP.

Figure 7 shows thermal trends from experiment (panel a) and computation (panel b). The difference spectra shown in both panels are in reasonable agreement with each other, indicating that the NRIXS measurements and s-TDEP calculations capture similar thermal trends in  $\text{Pd}_3\text{Fe}$ .

### C. Nonharmonic Behavior

The experimental nonharmonic behavior was analyzed by comparing the measured  $^{57}\text{Fe}$  pDOS with Fe pDOS curves predicted by quasiharmonic (QH) approximations. The experimental QH phonon frequencies  $\omega_i^{\text{QH}}(T)$  were calculated with the Grüneisen parameter model (referred to as the “QH  $\gamma_T$  Model”), a QH model using a thermal Grüneisen parameter  $\bar{\gamma}_T$ , averaged for all phonon modes:

$$\omega_i^{\text{QH}}(T) = \omega_i^{298\text{K}} \left( 1 - \bar{\gamma}_{\text{th}} \frac{V_T - V_{298\text{K}}}{V_{298\text{K}}} \right), \quad (14)$$

with the 298 K  $^{57}\text{Fe}$  phonons used for scaling the Grüneisen parameter in the QH  $\gamma_T$  model. The volumes at elevated temperatures  $V_T$  were calculated from the lattice parameters determined from our synchrotron XRD measurements, together with lattice parameters reported



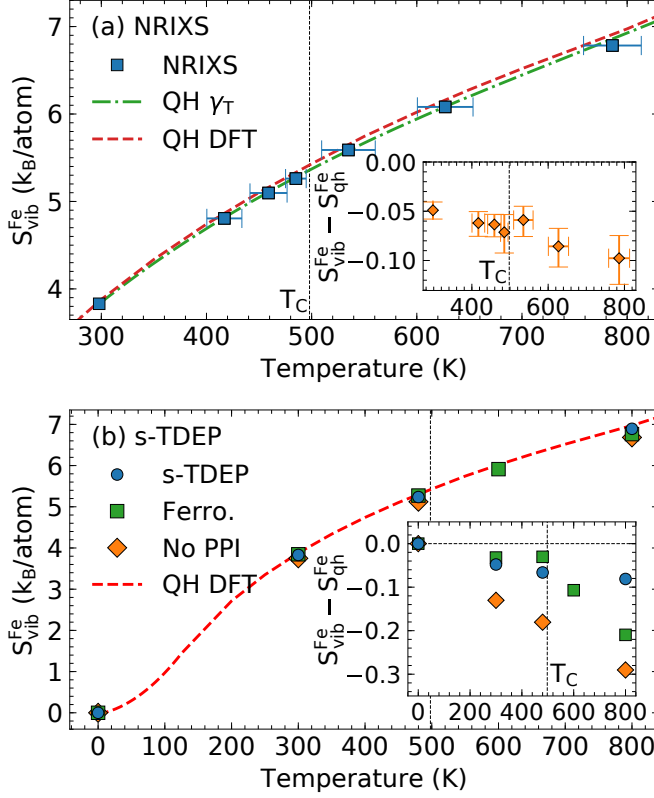


FIG. 8. (a) The Fe partial vibrational entropy from the NRIXS measurements compared with the entropy from the Grüneisen parameter model (QH  $\gamma_T$ ) and the QH DFT model. (b) The s-TDEP Fe partial vibrational entropy calculated for Pd<sub>3</sub>Fe with changing magnetic order (blue), ferromagnetic order (green), and the absence of phonon-phonon interactions (orange). The red line is the entropy from the QH DFT model. The insets in (a) and (b) show the nonharmonic contributions to the vibrational entropy.

by Jääskeläinen [28]. The thermal Grüneisen parameter was calculated from bulk properties of Pd<sub>3</sub>Fe:

$$\bar{\gamma}_{\text{th}}(T) = \frac{\alpha(T)K_T(T)\nu(T)}{C_V(T)}, \quad (15)$$

where  $K_T(T)$  is the bulk modulus,  $\alpha(T)$  is the linear thermal expansion,  $\nu(T)$  is the crystalline volume per atom, and  $C_V(T)$  is the heat capacity at constant volume. The quantities  $\alpha(T)$  and  $\nu(T)$  were calculated from volumes obtained from synchrotron XRD and from Jääskeläinen. The heat capacity was calculated by integrating the total phonon DOS calculated by s-TDEP. The bulk modulus was previously determined by Winterrose through energy-dispersive x-ray diffraction [20].

The average Fe phonon energies from the QH  $\gamma_T$  and QH DFT models are plotted in Fig. 5. The Fe phonons calculated with the two QH models soften more strongly with temperature than the NRIXS <sup>57</sup>Fe pDOS, indicating that there is a nonharmonic stiffening in Pd<sub>3</sub>Fe opposing the softening from thermal expansion.

Thermodynamic consequences of nonharmonic

phonons were assessed by calculating the Fe partial vibrational entropy  $S_{\text{vib}}^{\text{Fe}}$ , which contributes to the total thermodynamic entropy. This  $S_{\text{vib}}^{\text{Fe}}$  is obtained from the Fe pDOS as:

$$S_{\text{vib}}^{\text{Fe}}(T) = 3k_B \int g_T^{\text{Fe}}(\varepsilon) \{ (n+1) \ln(n+1) - n \ln(n) \} d\varepsilon, \quad (16)$$

where  $k_B$  is the Boltzmann constant,  $g_T^{\text{Fe}}(E)$  is the Fe pDOS at temperature  $T$ , and  $n$  is a Planck distribution evaluated at  $T$  for a given energy  $E$ . This expression provides accurate entropy values that include both quasi-harmonic effects and nonharmonic effects [59].

The  $S_{\text{vib}}^{\text{Fe}}(T)$  are plotted in Fig. 8(a). The quasi-harmonic vibrational entropy  $S_{\text{qh}}^{\text{Fe}}$ , also shown in the figure, was calculated by substituting the Fe pDOS from the QH  $\gamma_T$  and QH DFT models into Eq. 16. The agreement is surprisingly good, considering that the QH model neglects so many nonharmonic effects, including those shown in Fig. 8(b).

Fig. 8(b) shows the Fe partial vibrational entropy calculated with the phonons calculated with s-TDEP, together with the Fe partial vibrational entropy without effects from PPI. This quantity, labeled “No PPI,” was calculated by substituting the Fe pDOS calculated with Eq. 6 into Eq. 16. Also shown in the figure is the Fe partial vibrational entropy for ferromagnetic Pd<sub>3</sub>Fe. These quantities were compared with the quasi-harmonic entropy calculated from the QH DFT model.

The  $S_{\text{vib}}^{\text{Fe}}$  of Pd<sub>3</sub>Fe calculated with s-TDEP is lower than what is expected from the QH DFT model by 0.08  $k_B/\text{atom}$  at 800 K. The inclusion of PPI increases  $S_{\text{vib}}^{\text{Fe}}$  of Pd<sub>3</sub>Fe by 0.2  $k_B/\text{atom}$  at 800 K. The change in  $S_{\text{vib}}^{\text{Fe}}$  from ferromagnetic Pd<sub>3</sub>Fe to Pd<sub>3</sub>Fe with magnetic disorder increases from roughly  $-0.03 k_B/\text{atom}$  around the Curie temperature to roughly 0.1  $k_B/\text{atom}$  at 800 K. This happens as the deviation from quasi-harmonicity sharply increases for ferromagnetic Pd<sub>3</sub>Fe past the Curie temperature.

## IV. DISCUSSION

### A. Magnon-Phonon Interaction

The increase in Fe partial vibrational entropy with decreasing magnetization at 800 K arises from the softening of Fe vibrational energies with the magnetic transition. A more in-depth analysis of this softening with decreasing magnetization is performed by comparing the 800 K phonon dispersions for both ferromagnetic and paramagnetic Pd<sub>3</sub>Fe, as shown in Fig. 9.

A number of vibrational modes in Pd<sub>3</sub>Fe undergo energy shifts with the randomization of the Fe magnetic moment orientations, particularly the two optical modes at the X symmetry point highlighted in Fig. 9. The softening of these modes contributes to the softening of the high-energy peak in the Fe partial phonon DOS



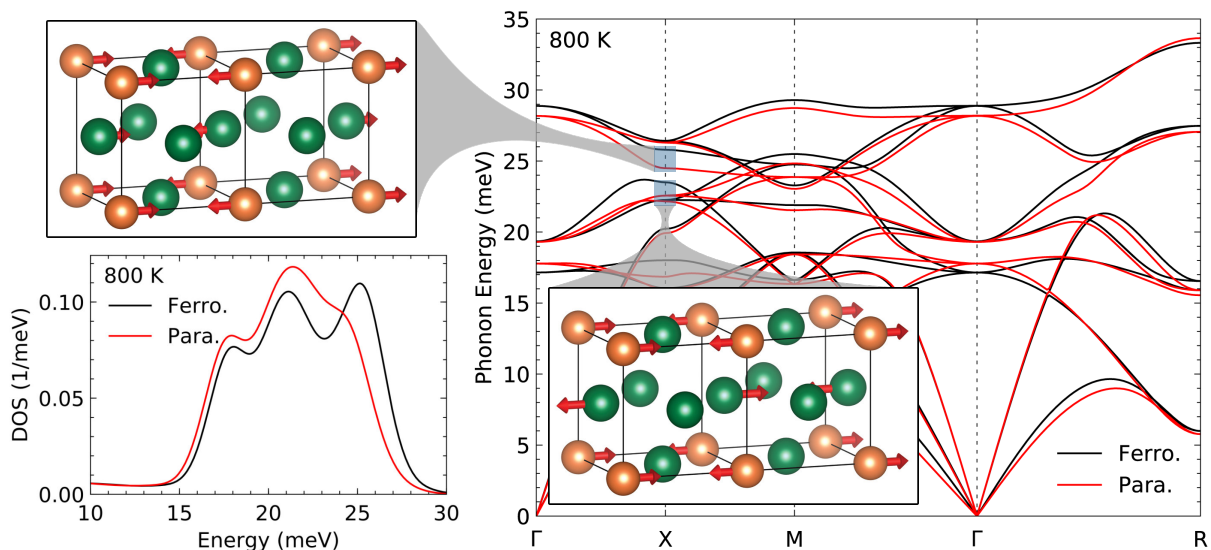


FIG. 9. Calculated phonon dispersions for the ferromagnetic and paramagnetic states at 800 K. The dispersions displayed do not include effects from phonon-phonon interactions. Displacement patterns are shown for two high-energy optical phonon modes that soften with decreasing magnetization. The orange and green spheres represent Fe and Pd atoms, respectively. The Fe partial phonon DOS curves of  $\text{Pd}_3\text{Fe}$  calculated with the s-TDEP method for the ferromagnetic and paramagnetic states at 800 K are shown in the lower left.

with decreasing magnetization. By testing the sensitivity of the phonon dispersions to changes in each of the quadratic force constants obtained from the fit of Eq. 1 to the Born-Oppenheimer surface, we found that these two modes soften with the weakening of the Fe–Fe second-nearest-neighbor (2NN) longitudinal force constants, which weaken by about 50% from the ferromagnetic state to the paramagnetic state at 800 K. This behavior is consistent with the atomic displacement patterns for the optical modes, which involve the motions of adjacent (100) planes of Fe atoms in opposite [100] directions. The softening of these modes coincides with a change in the interactions between the closest-neighbor magnetic atoms due to the loss of short-range magnetic order past the Curie temperature.

The average  $^{57}\text{Fe}$  phonon energies from the NRIXS measurements change slowly below the Curie temperature. The s-TDEP calculations for  $\text{Pd}_3\text{Fe}$  and ferromagnetic  $\text{Pd}_3\text{Fe}$  show that the thermal evolution of the optical phonons depends on whether the magnetization changes with thermal fluctuations. A thermal optical phonon stiffening in ferromagnetic  $\text{Pd}_3\text{Fe}$  counteracts the phonon softening from thermal expansion. This behavior is observed in the NRIXS measurements from 298 to 485 K, where  $\text{Pd}_3\text{Fe}$  still maintains short-range magnetic order. In this case, the short-wavelength optical modes do not soften strongly with temperature, consistent with their behavior in a material with full magnetic order. Beyond the Curie temperature, where there is both long- and short-range magnetic disorder, the change in Fe–Fe interactions cancels this ferromagnetic stiffening of the short-wavelength optical phonons.

## B. Phonon-Phonon Interaction

The s-TDEP calculations of the phonon DOS of  $\text{Pd}_3\text{Fe}$  show that anharmonicity has significant effects on the thermodynamics of the material, as indicated by the increase in the Fe partial vibrational entropy by up to  $0.2 k_B/\text{atom}$  at 800 K. The anharmonic phonon shifts and broadenings can be studied in more detail with the phonon spectral functions  $S(\mathbf{q}, E)$ , the spectra of lattice excitations that can be interpreted as phonon modes broadened and shifted by phonon-phonon interactions. The spectral function is calculated with  $\omega_{\mathbf{q}s}$ , the phonon dispersion from quadratic force constants, and the real and imaginary components of the phonon self energy from Eq. 7 and 8:

$$S(\mathbf{q}, E) \propto \sum_s \frac{2\omega_{\mathbf{q}s}\Gamma_{\mathbf{q}s}(\Omega)}{[\Omega^2 - \omega_{\mathbf{q}s}^2 - 2\omega_{\mathbf{q}s}\Delta_{\mathbf{q}s}(\Omega)]^2 + 4\omega_{\mathbf{q}s}^2\Gamma_{\mathbf{q}s}^2(\Omega)}. \quad (17)$$

The spectral functions shown in Fig. 10 were calculated at multiple temperatures. The 0 K spectral function is in good agreement with the phonon dispersion measured with inelastic neutron scattering at 80 K by Stirling [61]. The significant phonon broadening and shifts in the spectral functions at higher temperatures come from many decay channels available to the phonons in the twelve branches.

We examined the lineshapes of phonon modes at specific  $\mathbf{q}$  points in the Brillouin zone, including the 800 K lineshapes of the phonon modes affected by the magnetic transition at the X symmetry point, shown in Fig. 11. What was unusual was a double-peak structure of one

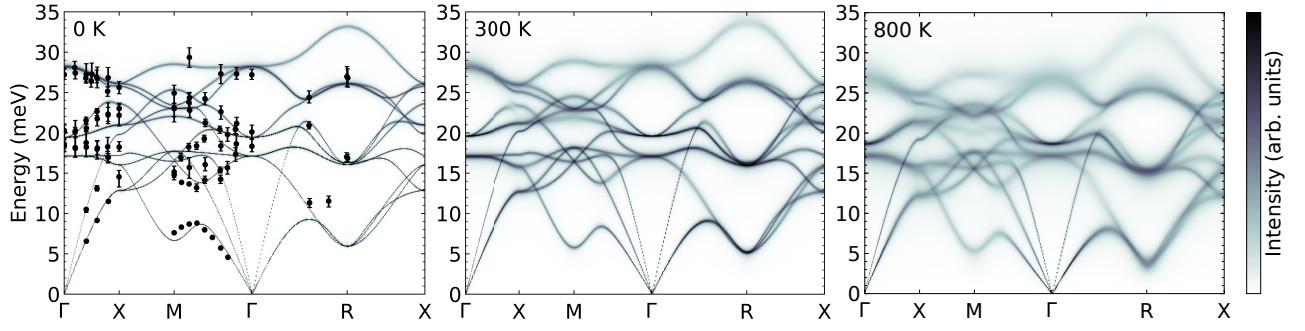


FIG. 10.  $\text{Pd}_3\text{Fe}$  spectral functions (logarithmic intensity scale) calculated with s-TDEP along the high-symmetry directions at 0, 300, and 800 K. Measurements of the 80 K phonon dispersion by inelastic neutron scattering [61] are shown on top of the 0 K spectral function.

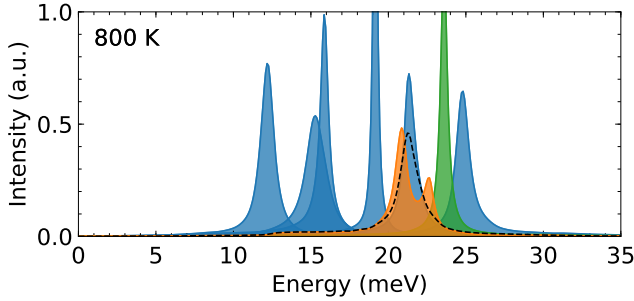


FIG. 11.  $\text{Pd}_3\text{Fe}$  phonon lineshapes at the X high symmetry point at 800 K. The orange and green peaks are the optical modes that shift with changing magnetic order. The black dashed peak is the lineshape of the optical mode after the Pd–Pd 1NN cubic force constant is set to zero.

of these high-energy optical modes. Phonon modes with lineshapes that are characterized by a single peak broadened by a Lorentzian are mildly anharmonic, whereas phonon modes that have unusual lineshapes are more strongly anharmonic [62, 63].

To study the nature of the double peak of the high-energy phonon mode at X, we analyzed the cubic irreducible force constants responsible for three-phonon interactions. The lineshapes at the X point were calculated when an irreducible force constant was set to zero. It was found that zeroing the cubic force constants for the Fe–Pd first nearest neighbors (1NN) along the  $\langle 110 \rangle$  directions partially removes the double-peak structure, but zeroing the cubic force constants for the Pd–Pd 1NN along the  $\langle 110 \rangle$  directions fully transforms the double-peak lineshape to a single Lorentzian peak, shown in Fig. 11.

These force constants are related to the movement of Fe and Pd atoms in the  $[100]$  direction against the adjacent stationary (200) planes of Pd atoms. As shown in the displacement pattern of the vibrational mode in Fig. 9, (100) planes of Fe atoms and (100) of Pd atoms alternate in oscillating against the stationary (200) planes of Pd atoms. The cubic interactions from the oscillation

of the (100) planes of Pd atoms against the (200) Pd planes more strongly contributes to the unusual phonon lineshape. We suggest that the palladium atoms dominate the anharmonic phonon-phonon interactions in  $L1_2$ -ordered  $\text{Pd}_3\text{Fe}$ . This is consistent with how fcc Pd shows strong PPI at high temperatures [64].

## V. CONCLUSIONS

Nuclear resonant inelastic x-ray scattering was used to measure the  $^{57}\text{Fe}$  partial phonon DOS of  $L1_2$ -ordered  $\text{Pd}_3\text{Fe}$  from room temperature through the Curie transition. The iron partial vibrational entropy at temperatures far from the Curie transition was observed to be approximately what was predicted by the quasiharmonic approximation owing to a cancellation of effects. A non-harmonic phonon stiffening opposed the expected softening from thermal expansion below the Curie temperature. Similar trends were observed from first-principles calculations that couple the stochastically-initialized temperature dependent effective potential (s-TDEP) method with magnetic special quasirandom structures (SQSs) of noncollinear magnetic moments.

The s-TDEP calculations showed that phonon-phonon interactions (PPI) contribute to the softening and broadening of the phonon spectra at elevated temperatures. A high-energy optical mode at the X symmetry point was calculated to have a double-peak lineshape. The first-nearest-neighbor Pd–Pd cubic interactions strongly contribute to this unusual lineshape, highlighting the strong contribution of the majority Pd atoms to the phonon anharmonicity in  $\text{Pd}_3\text{Fe}$ .

The calculations also showed that high-energy optical modes soften with decreasing magnetization, so a ferromagnetic optical phonon stiffening is lost. This softening of optical modes originates with how the randomization of orientations of the Fe magnetic moments alters the short-range Fe–Fe interactions, softening the Fe–Fe second-nearest-neighbor force constants. The dependence of these optical vibrational modes on the magnetic

transition can be understood as how magnon-phonon interactions alter lattice vibrations at elevated temperatures.

## ACKNOWLEDGMENTS

This work was supported by the Department of Energy (DOE) through the Capital/DOE Alliance Center, funded by the Department of Energy/National Nuclear Security Administration under Grant No. DE-NA-0002006. The calculations performed herein were made possible by resources of the National Energy Re-

search Scientific Computing Center, a DOE Office of Science User Facility supported by the Office of Science of the U.S. Department of Energy under Contract No. DE-AC02-05CH11231. Portions of this work were performed at HPCAT (Sector 16), Advanced Photon Source (APS), Argonne National Laboratory. HPCAT operations are supported by DOE-NNSA under Award No. DE-NA0001974, with partial instrumentation funding by NSF. The Advanced Photon Source is a U.S. Department of Energy (DOE) Office of Science User Facility operated for the DOE Office of Science by Argonne National Laboratory under Contract No. DE-AC02-06CH11357.

- <sup>1</sup> I. A. Abrikosov, A. V. Ponomareva, P. Steneteg, S. A. Barannikova, and B. Alling, *Curr. Opin. Solid State Mater. Sci.* **20**, 85 (2016).
- <sup>2</sup> P. Steneteg, B. Alling, and I. A. Abrikosov, *Phys. Rev. B* **85**, 144404 (2012).
- <sup>3</sup> N. Shulumba, B. Alling, O. Hellman, E. Mozafari, P. Steneteg, M. Odén, and I. A. Abrikosov, *Phys. Rev. B* **89**, 174108 (2014).
- <sup>4</sup> F. Körmann, A. Dick, B. Grabowski, T. Hickel, and J. Neugebauer, *Phys. Rev. B* **85**, 125104 (2012).
- <sup>5</sup> F. Körmann, B. Grabowski, B. Dutta, T. Hickel, L. Mauger, B. Fultz, and J. Neugebauer, *Phys. Rev. Lett.* **113**, 165503 (2014).
- <sup>6</sup> F. Körmann, A. A. H. Breidi, S. L. Dudarev, N. Dupin, G. Ghosh, T. Hickel, P. Korzhavyi, J. A. Muñoz, and I. Ohnuma, *Physica Status Solidi B* **251**, 53 (2014).
- <sup>7</sup> Y. Ikeda, F. Körmann, B. Dutta, A. Carreras, A. Seko, J. Neugebauer, and I. Tanaka, *npj Comput. Mater.* **4**, 7 (2018).
- <sup>8</sup> V. P. Antropov, M. I. Katsnelson, M. vanSchilfgaarde, and B. N. Harmon, *Phys. Rev. Lett.* **75**, 729 (1995).
- <sup>9</sup> V. P. Antropov, M. I. Katsnelson, B. N. Harmon, M. vanSchilfgaarde, and D. Kusnezov, *Phys. Rev. B* **54**, 1019 (1996).
- <sup>10</sup> B. Skubic, J. Hellsvik, L. Nordström, and O. Eriksson, *J. Phys. Condens. Matter* **20**, 315203 (2008).
- <sup>11</sup> L. Mauger, M. S. Lucas, J. A. Muñoz, S. J. Tracy, M. Kresch, Y. Xiao, P. Chow, and B. Fultz, *Phys. Rev. B* **90**, 064303 (2014).
- <sup>12</sup> T. Sohmura, R. Oshima, and F. E. Fujita, *Scr. Metall.* **14**, 855 (1980).
- <sup>13</sup> M. Sugiyama, S. Harada, and R. Oshima, *Scr. Metall.* **19**, 315 (1985).
- <sup>14</sup> Y. Tsunoda and R. Abe, *Phys. Rev. B* **55**, 11507 (1997).
- <sup>15</sup> R. Abe, Y. Tsunoda, M. Nishi, and K. Kakurai, *J. Phys. Condens. Matter* **10**, L79 (1998).
- <sup>16</sup> B. Dutta, S. Bhandary, S. Ghosh, and B. Sanyal, *Phys. Rev. B* **86**, 024419 (2012).
- <sup>17</sup> Y. O. Kvashnin, S. Khmelevskiy, J. Kudrnovský, A. N. Yaresko, L. Genovese, and P. Bruno, *Phys. Rev. B* **86**, 174429 (2012).
- <sup>18</sup> A. Kussmann and K. Jessen, *J. Phys. Soc. Japan Suppl.* **17B1**, 136 (1962).
- <sup>19</sup> G. Longworth, *Phys. Rev.* **172**, 572 (1968).
- <sup>20</sup> M. L. Winterrose, M. S. Lucas, A. F. Yue, I. Halevy, L. Mauger, J. A. Muñoz, J. Hu, M. Lerche, and B. Fultz, *Phys. Rev. Lett.* **102**, 237202 (2009).
- <sup>21</sup> M. L. Winterrose, L. Mauger, I. Halevy, A. F. Yue, M. S. Lucas, J. A. Muñoz, H. Tan, Y. Xiao, P. Chow, W. Sturhahn, T. S. Toellner, E. E. Alp, and B. Fultz, *Phys. Rev. B* **83**, 134304 (2011).
- <sup>22</sup> See Supplemental Material, which includes Ref. [23], at [URL will be provided by the publisher] for technical details and results of x-ray diffraction and Mössbauer spectroscopy, raw NRIXS scattering spectra and the multiphonon contributions, Lamb-Mössbauer factors, and a comparison of the scattering data to past measurements.
- <sup>23</sup> A. P. Hammersley, S. O. Svensson, M. Hanfland, A. N. Fitch, and D. Häusermann, *High Press. Res.* **14**, 235 (1996).
- <sup>24</sup> A. Chumakov and W. Sturhahn, *Hyperfine Interact.* **123-124**, 781 (1999).
- <sup>25</sup> W. Sturhahn and V. Kohn, *Hyperfine Interact.* **123-124**, 367 (1999).
- <sup>26</sup> W. Sturhahn, *Hyperfine Interact.* **125**, 149 (2000).
- <sup>27</sup> W. Sturhahn and J. M. Jackson, *Geophys. Soc. Am. Special Papers* **421**, 157 (2007).
- <sup>28</sup> J. Jääskeläinen and E. Suoninen, *Phys. Status Solidi A* **63**, 241 (1981).
- <sup>29</sup> O. Hellman, I. A. Abrikosov, and S. I. Simak, *Phys. Rev. B* **84**, 180301 (2011).
- <sup>30</sup> O. Hellman, P. Steneteg, I. A. Abrikosov, and S. I. Simak, *Phys. Rev. B* **87**, 104111 (2013).
- <sup>31</sup> O. Hellman and I. A. Abrikosov, *Phys. Rev. B* **88**, 144301 (2013).
- <sup>32</sup> N. Shulumba, O. Hellman, and A. J. Minnich, *Phys. Rev. B* **95**, 014302 (2017).
- <sup>33</sup> D. West and S. K. Estreicher, *Phys. Rev. Lett.* **96**, 115504 (2006).
- <sup>34</sup> I. Errea, M. Calandra, and F. Mauri, *Phys. Rev. B* **89**, 064302 (2014).
- <sup>35</sup> N. Shulumba, O. Hellman, and A. J. Minnich, *Phys. Rev. Lett.* **119**, 185901 (2017).
- <sup>36</sup> D. S. Kim, O. Hellman, J. Herriman, H. L. Smith, J. Y. Y. Lin, N. Shulumba, J. L. Niedziela, C. W. Li, D. L. Abernathy, and B. Fultz, *Proc. Natl. Acad. Sci. USA* **115**, 1992 (2018).
- <sup>37</sup> P. E. Blochl, *Phys. Rev. B* **50**, 17953 (1994).
- <sup>38</sup> G. Kresse and J. Furthmüller, *Phys. Rev. B* **54**, 11169 (1996).

- <sup>39</sup> G. Kresse and J. Furthmüller, *Comput. Mat. Sci.* **6**, 15 (1996).
- <sup>40</sup> H. Monkhorst and J. Pack, *Phys. Rev. B* **13**, 5188 (1976).
- <sup>41</sup> J. P. Perdew, K. Burke, and M. Ernzerhof, *Phys. Rev. Lett.* **77**, 3865 (1996).
- <sup>42</sup> S. J. Pickart and R. Nathans, *J. Appl. Phys.* **33**, 1336 (1962).
- <sup>43</sup> V. A. Tsurin and A. Z. Men'shikov, *Phys. Met. Metallogr.* **45**, 82 (1978).
- <sup>44</sup> A. Z. Men'shikov and V. A. Tsurin, *Phys. Met. Metallogr.* **47**, 68 (1979).
- <sup>45</sup> A. A. Maradudin and A. E. Fein, *Phys. Rev.* **128**, 2589 (1962).
- <sup>46</sup> R. A. Cowley, *Rev. Prog. Phys.* **31**, 123 (1968).
- <sup>47</sup> A. Zunger, S.-H. Wei, L. G. Ferreira, and J. E. Bernard, *Phys. Rev. Lett.* **65**, 353 (1990).
- <sup>48</sup> B. Alling, T. Marten, and I. A. Abrikosov, *Phys. Rev. B* **82**, 184430 (2010).
- <sup>49</sup> J. Hubbard, *Phys. Rev. B* **19**, 2626 (1979).
- <sup>50</sup> J. Hubbard, *Phys. Rev. B* **20**, 4584 (1979).
- <sup>51</sup> J. Hubbard, *Phys. Rev. B* **23**, 5974 (1981).
- <sup>52</sup> H. Hasegawa, *J. Phys. Soc. Jpn.* **46**, 1504 (1979).
- <sup>53</sup> H. Hasegawa, *J. Phys. Soc. Jpn.* **49**, 178 (1980).
- <sup>54</sup> B. L. Gyorffy, A. J. Pindor, J. Staunton, G. M. Stocks, and H. Winter, *J. Phys. F: Met. Phys.* **15**, 1337 (1985).
- <sup>55</sup> G. Inden, Project Meeting CALPHAD V (1976), pp. 1-13.
- <sup>56</sup> M. D. Kuz'min, *Phys. Rev. Lett.* **94**, 107204 (2005).
- <sup>57</sup> W. Sturhahn and E. Gerdau, *Phys. Rev. B* **49**, 9285 (1994).
- <sup>58</sup> L. Mauger, J. E. Herriman, O. Hellman, S. J. Tracy, M. S. Lucas, J. A. Muñoz, Y. Xiao, J. Li, and B. Fultz, *Phys. Rev. B* **95**, 024308 (2017).
- <sup>59</sup> D. C. Wallace, *Thermodynamics of Crystals* (Dover Publications, Mineola, New York, 1998).
- <sup>60</sup> D. C. Wallace, *Statistical physics of crystals and liquids. A guide to highly accurate equations of state* (World Scientific, Singapore, 2002).
- <sup>61</sup> W. G. Stirling, R. A. Cowley, and M. W. Stringfellow, *J. Phys. F: Met. Phys.* **2**, 421 (1972).
- <sup>62</sup> O. Delaire, J. Ma, K. Marty, A. F. May, M. A. McGuire, M.-H. Du, D. J. Singh, A. Podlesnyak, G. Ehlers, M. D. Lumsden, and B. C. Sales, *Nat. Mater.* **10**, 614 (2011).
- <sup>63</sup> C. W. Li, O. Hellman, J. Ma, A. F. May, H. B. Cao, X. Chen, A. D. Christianson, G. Ehlers, D. J. Singh, B. C. Sales, and O. Delaire, *Phys. Rev. Lett.* **112**, 175501 (2014).
- <sup>64</sup> Y. Shen, C. W. Li, X. Tang, H. L. Smith, and B. Fultz, *Phys. Rev. B* **93**, 214303 (2016).